Road-Speed Estimation Using Convolutional Neural Networks and Simulated ϕ-OTDR Traces

R. A. Colares and D. A. A. Mello

***Abstract*— We investigate distributed fiber optic sensing and machine-learning-based image analysis for road-speed estimation. Synthetic phase-sensitive optical time-domain reflectometer (ϕ-OTDR) traces are generated by the simulation of random road features such as car density and speed. Consecutive ϕ-OTDR traces are stacked generating images that are submitted to a convolutional neural network (CNN) for classification. The evaluated CNN-based classifier exhibits high accuracy at sufficiently high car densities.**

***Keywords*— Distributed fiber optic sensing, phase-sensitive optical time-domain reflectometer, convolutional neural network classifier, road-speed estimation, traffic control.**

I. Introduction

Most current long-haul optical links have dedicated out-of-band optical time-domain reflectometers (OTDRs) using broadband sources for online troubleshooting and maintenance. While a conventional OTDR allows for detecting reflections and fiber losses, a phase-sensitive OTDR (ϕ-OTDR) employs a coherent light source to detect phase changes along the fiber. The high sensitivity of ϕ-OTDRs to vibration and strain has enabled the use of legacy optical fibers as distributed fiber optic sensors [1] for several applications [2]–[8]. Recent works have demonstrated that optical fibers installed alongside roads can be particularly used for road-traffic monitoring [9]. These works stack ϕ-OTDR traces to generate images illustrating the traffic evolution along distance and time. Image generation is then followed by machine-learning-based (ML-based) image processing for estimating parameters such as car position, speed, weight, and traffic density [10]. Furthermore, the vibration caused by vehicles traversing degraded pavements generates ϕ-OTDR anomalies that can be used to detect holes and excessive roughness. In [10], traffic information is obtained by normalization, morphological operations, Gaussian smoothing and blob analysis of ϕ-OTDR stacked traces. The road roughness level is evaluated by support vector machines (SVMs) [10].

In spite the intense experimental research activity in distributed sensing using legacy fibers, the simulation of these systems for the development of related ML-based techniques has not been addressed. This paper evaluates convolutional neural networks (CNNs) for road-speed estimation. Although we focus on road speed, other parameters can be estimated using the same framework. Synthetic ϕ-OTDR traces are generated by simulation using a validated model based on refractive index perturbations [14]. Vehicles are randomly generated to produce desired mean road speeds and car densities. The simulated traces are stacked and processed by a CNN for image classification and road-speed estimation, followed by signal-to-noise (SNR) analysis and discussion. The remainder of this paper is structured as follows. Section II presents the system setup containing the ϕ-OTDR model and the CNN-based classifier. The simulation results are presented and discussed in Section III. Lastly, Section IV concludes the paper.

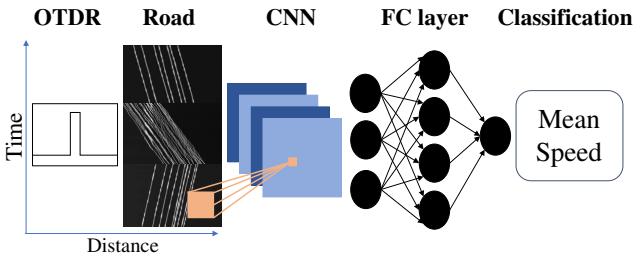

Fig. 1: Road-speed estimation framework. ϕ-OTDR traces are simulated and stacked to build images. Images are processed by a CNN followed by a fully connected layer operating as a classifier.

II. System Setup

The evaluated system setup is depicted in Fig. 1. First, a ϕ-OTDR simulation model generates synthetic backscattering traces. Multiple ϕ-OTDR traces are stacked, generating images representing the road traffic condition. The generated image is subsequently submitted to a CNN classifier for road-speed estimation. The following sections detail the simulation model and the CNN classifier.

A. ϕ-OTDR model

The electric field of the backscattered light is modeled assuming a longitudinal waveguide containing a set of discrete frozen-in inhomogeneities of uniform length Δz, interacting with a light pulse with length d [11]–[13], as depicted in Fig. 2. The pulse length is assumed to be equivalent to the spatial resolution of ϕ-OTDR, obtained as [14]

Robson Assis Colares, Department of Communications, Unicamp, Campinas-SP, e-mail: robcolares@ieee.org; Darli Augusto de Arruda Mello, Department of Communications, Unicamp, Campinas-SP, e-mail: darli@unicamp.br. This work was supported by the National Council for Scientific and Technological Development (CNPq) grant 131336/2020-7 and by the São Paulo Research Foundation (FAPESP), grants 2015/24517-8 and 2015/24341- 7. This study was financed in part by the Coordenação de Aperfeiçoamento de Pessoal de Nivel Superior - Brasil (CAPES) - Finance Code 001.

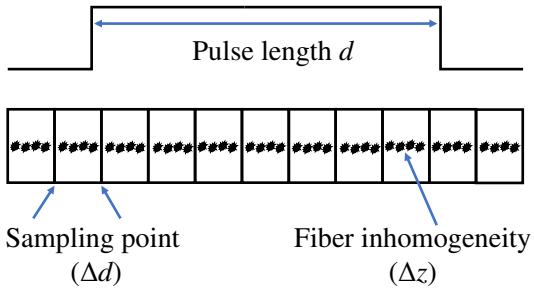

Fig. 2: Discrete 1D model of the optical fiber for ϕ-OTDR sensing. Several inhomogeneities of size Δz inside the pulse length impact on the intensity of ϕ-OTDR.

$$d = \frac{c\tau}{2n_{\text{ave}}}, \tag{1}$$

where c is the speed of light in vacuum, τ is the pulse width in the time domain, and n_{ave} is the average effective refractive index.

As there is interference among the light backscattered from different inhomogeneities within the optical pulse, the obtained trace shows a stochastically varying amplitude. The contributions of the incident pulse electric field E_{in}, reflected within pulse length d starting at position z, are summed up at the photodetector as [14]

$$E(z) = e^{-\alpha z + j2\phi(z)} \sum_{m=0}^{M} E_{\text{in}}(m) r(z + m\Delta z) e^{j2\phi(z+m\Delta z)}, \tag{2}$$

where α is the power attenuation coefficient, $\phi(z)$ is the accumulated optical phase from the fiber input to position z, $M = d/\Delta z$ is the number of scattering segments within a pulse, and $r(z+m\Delta z)$ is the reflection coefficient of segment m. $\phi(z)$ is obtained by integration of propagation constant β, thus

$$\phi(z) = \int_0^z \beta(x)dx = 2\pi \frac{\nu_0}{c} \int_0^z n(x)dx, \tag{3}$$

where ν_0 is the central optical frequency of the incident field. The local effective refractive index $n(z)$ is defined as

$$n(z) = n_{\text{ave}} + \Delta n(z), \tag{4}$$

where $\Delta n(z)$ is the randomly generated local index variation. In (2), losses within the pulse width are neglected. In general, ϕ-OTDR architectures locate refractive index perturbations by analyzing time-varying anomalies in $|E(z)|^2$.

In the simulation of $\Delta n(z)$, the fiber is considered a long grating with random amplitude and pitch [14], where light is partially reflected at the interface between inhomogeneities. The refractive index coherence length in an optical fiber is in the order of 10 nm [15], making the evaluation of (2) computationally expensive as millions and even billions of inhomogeneities can be found in few kilometers of fiber. To simplify the computational workload, $\Delta n(z)$ is replaced by a discretized equivalent $\Delta n'(z)$ at each sampling point, spaced by Δd [16].

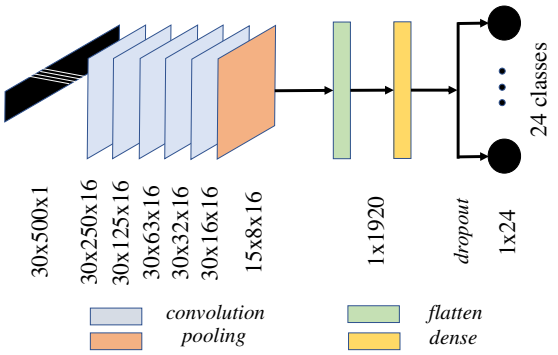

Fig. 3: CNN architecture used for image classification. Images are submitted to convolutional layers followed by pooling and dense layers, then classified into 24 classes. Dropout is used for regularization.

The reflection coefficient $r(z)$ is calculated using the normal incidence case of the Fresnel equation. The reflection coefficient at position z_i depends on the refractive index at positions z_i and z_{i+1}

$$r(z_i) = \frac{n(z_i) - n(z_{i+1})}{n(z_i) + n(z_{i+1})}. \tag{5}$$

In this work, we assume that strains generate an additional refractive index change, Δn_ε, given by [14]

$$\Delta n_\varepsilon = n_{\text{ave}}(1 - 0.1 n_{\text{ave}}^2)\varepsilon, \tag{6}$$

where ε is the applied strain.

A reference trace is obtained with random $\Delta n'(z)$ representing an unperturbed fiber, and perturbations with amplitude ε are locally added representing car movements along the fiber. Sequential traces of $|E(z)|^2$ are subtracted, allowing to obtain the vibration position. The traces are then stacked allowing image creation along time and distance. The generated images are then headed to a trained CNN model for speed estimation.

B. Neural network classification

The subtraction of the unperturbed and the perturbed ϕ-OTDR traces is normalized and transformed into a single vector of pixels (from 0 to 255, grayscale), and then concatenated as power images along time and distance to represent car movements along the road. After image generation, the actual mean speed is used for labeling. The dataset contains 24000 labeled images, separated into 24 balanced classes from 0 to 120 km/h. For example, the first class corresponds to images whose labeled mean speed is between 0 and 5 km/h. The generated images are then separated into 24 balanced classes and submitted to a CNN [17], [18] for training and validation. 80% of the images are used for training and 20% for validation. Additionally, extra 960 unseen images are used for testing. New images are submitted to the trained CNN for mean speed classification.

The CNN architecture is depicted in Fig. 3. Rescaling (from 0–255 to 0–1) is used before the CNN to avoid strong

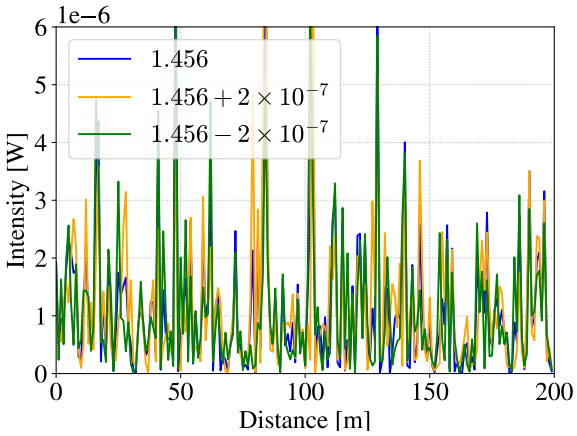

Fig. 4: Simulated ϕ-OTDR traces for three different average refractive indexes. Even a small change in refractive index or wavelength leads to changes in intensity of backscattered light.

fluctuations during training and for faster convergence. A batch size of 16 is empirically chosen due to better classification rates. The neural network is designed with five convolutional layers with 16 filters each, using a 3x3 kernel size for feature extraction. A stride of 1 and 2 is applied for vertical and horizontal filter displacement, respectively. The rectifier linear unit (ReLU) activation function is used for all layers, followed by a batch normalization layer.

After the last convolutional layer, a fully-connected layer (FC layer) with 100 hidden and 24 output neurons is used for classification. Softmax activation function is used in the output layer, providing a probability indicator for the corresponding output. Dropout is applied before hidden and output dense layers for regularization, by randomly deleting a fraction of neuronal connections. The CNN uses a learning rate of 0.001 and the categorical cross-entropy as a loss function. After training and hyperparameter tuning, the classified mean speed is compared with the labeled mean speed using 960 unseen images.

III. Results

Fig. 4 shows ϕ-OTDR traces for 1.456, 1.456 + 2×10^{-7} and 1.456 - 2×10^{-7} average refractive indexes. A variance of 2×10^{-6} is applied for index fluctuations [14] in all evaluated scenarios. As expected, subtle variations in the average refractive index lead to different traces in intensity. The ϕ-OTDR pulse peak power is set to 200 mW, according to [9]. The simulation setup considers the retrieval of one $\phi-$OTDR trace per second. Each image is composed by 30 lines, representing 30 ϕ-OTDR concatenated traces. The sampling interval Δd is set to 0.1 m, yielding 5000 data points in a 500-m road segment. Each 30×5000-data array is resized to 30×500 and transformed into images. A maximum car size of 4 m is considered with a 1-m minimum distance between cars, leading to a maximum car density of 200 cars/km. Cars are randomly generated aiming at a given car density. The position of each car is uniformly selected in a 1500-m segment, and only the last 500-m is used to generate images. This approach ensures that cars may enter the image within the 30-s time frame. The simulation ensures a car spacing of at least one meter. Each generated image corresponds to a specific speed V_0. The simulation parameters are summarized in Table I.

TABLE I: General Simulation Parameters

Parameter	Value
Car size	4 m
Fiber attenuation coefficient (α)	0.2 dB/km
Fiber average refractive index (n_{ave})	1.456
Index Variance ($\sigma^2_{\Delta n}$)	2×10^{-6}
Inhomogeneity size (Δz)	0.1 m
Maximum car density	200 cars/km
Maximum speed (V_{max})	120 km/h
Pulse duration (τ)	10 ns
Pulse peak power (P_0)	200 mW
Sampling Period (Δd)	0.1 m
Sampling Rate	1 GS/s
Vibration Amplitude (ε)	0.2 $\mu\varepsilon$
Wavelength (λ)	1550 nm

(a) Raw image with correct classification.

(b) Raw image with incorrect classification.

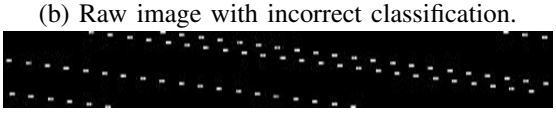

(c) Truncated image with correct classification.

Fig. 5: Examples of generated images. Image pre-processing techniques such as binarization and truncation lead to more discernible patterns in feature space, achieving better classification results. The exemplified mean speeds are (a) 7.50 km/h and (b,c) 62.55 km/h, respectively.

The statistical variation of refractive index generates outliers in subtracted traces with poor data point representation. To circumvent this problem and eliminate spurious peaks we truncate subtracted traces to 10 times the mean value. Fig. 5a shows an example of a correctly classified raw image, i.e., without truncation. An image corresponding to incorrect classification is shown in Fig. 5b, revealing unintelligible features related to mean speed. The same image after truncation is shown in Fig. 5c, revealing clear features related to mean speed. For comparison, a truncated image dataset reaches a classification accuracy higher than 93% with 1000 images per class. If raw images were used, at least 2000 images per class would be needed to reach similar result using the same architecture. The model was trained for 25 epochs. Fig. 6 shows training and validation loss and accuracy along the training process. It is possible to see that the validation loss (red line) and accuracy (blue line) cease to improve at the 20^{th} epoch, while training loss and accuracy barely improve, pointing to negligible overfitting after 20^{th} epoch. Due to high

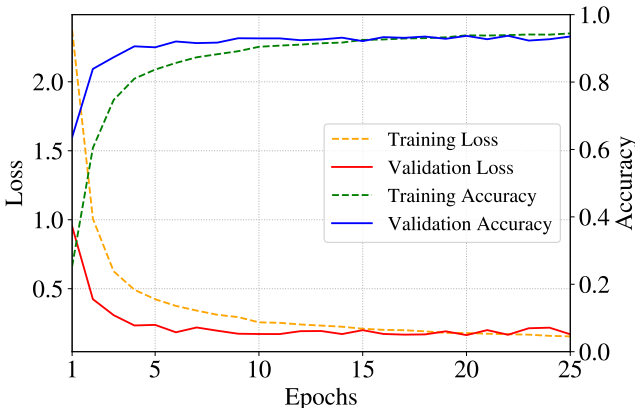

Fig. 6: Loss and accuracy curves for CNN training and validation. It can be inferred that after 20$^{\text{th}}$ epoch, no accuracy improvement is evidenced and overfitting is prone to occur.

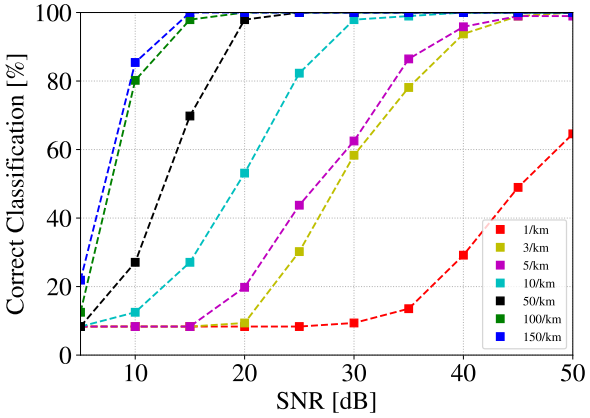

Fig. 8: Results of a CNN classifier applied to noise-added images (SNR from 0-50 dB). High classification accuracy is exhibited for 30-dB SNR and above.

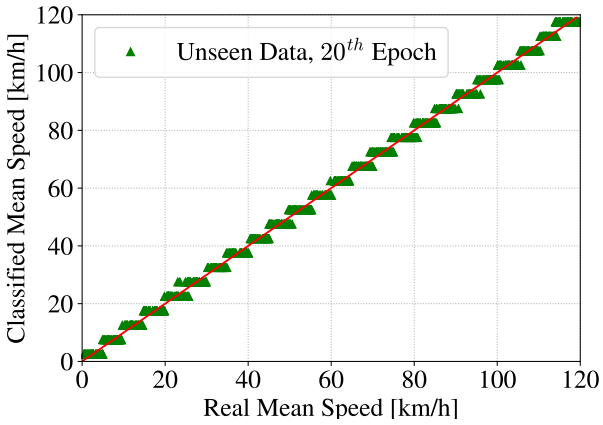

Fig. 7: Results of a CNN classifier applied to 960 unseen data balanced into 24 classes. It can be seen classification errors occur generally in neighbor classes.

validation accuracy and small loss, the model corresponding to the 20$^{\text{th}}$ epoch is used for classification.

Fig. 7 shows the performance of the road-speed classifier for 960 unseen images. A suitable performance is observed for the entire investigated range of investigated parameters, reaching 93.71% validation accuracy and classification errors occurring only in neighboring classes. 92.90% of correct classification is reached for unseen data. We observed that most errors correspond to images whose actual speed is in the threshold between classes.

We also investigate the robustness of the investigated classifier against noise. As there are several $\phi-$OTDR architectures, with and without amplification [19]–[22], and to better generalize the results, we evaluate the classifier performance under different SNR conditions. We generate SNR levels ranging from 0 dB to 50 dB considering additive white Gaussian noise (AWGN) added to the traces before subtraction. Fig. 8 presents the fraction of correctly classified images versus SNR for car densities of 1, 3, 5, 10, 50, 100 and 150 cars/km. As expected, at low SNRs and low car densities vertical patterns generated by refractive index fluctuations are more prominent than diagonal patterns generated by car movements, impairing pattern recognition. Poor performance is particularly observed at high speeds, where the low number of registered points impairs performance. This problem is alleviated when the car density is increased. Accordingly, we observe a higher classification rate is reached for higher car densities. The results of Fig. 8 reveal a high accuracy (100% in the investigated dataset) for car densities higher than 10 cars/kilometer and SNRs higher than 30 dB. The influence of the average car speed on the classification accuracy is shown in Fig 9(a)-(d). The accuracy is degraded at high speeds and low car densities due to the lack of data points available for feature recognition, dispersing pixels and impairing the straight-line-like aspect of the collected traces. Despite these limitations, 100% correct classification is reached for SNRs higher than 20 dB and more than 50 cars/kilometer.

IV. Conclusion

We evaluate a ϕ-OTDR-based sensing system for road-speed estimation based on CNNs. Synthetic ϕ-OTDR traces are simulated using a refractive index perturbation approach to represent car vibrations. Concatenated ϕ-OTDR traces form images representing traffic evolution along time and distance. These images are divided in 24 classes and processed by a CNN for training and validation. Image pre-processing using truncation leads to higher validation accuracies in smaller datasets. The simulated neural network exhibits a suitable performance in the simulated range of parameters, reaching 93.71% validation and 92.90% test accuracy over unseen data, where classification errors occur only on neighboring classes. SNR analysis is carried out by adding noise to ϕ-OTDR traces and submitting the subtraction of noisy images to a CNN for classification. We observe a high classification rate for car densities higher than 10 car/km and SNRs higher than 30 dB or car densities higher than 50 car/km and SNRs higher than 20 dB. Future works include the investigation of additional parameters and events such as road roughness, sudden deceleration, and the computation of the SNR for different $\phi-$OTDR architectures.

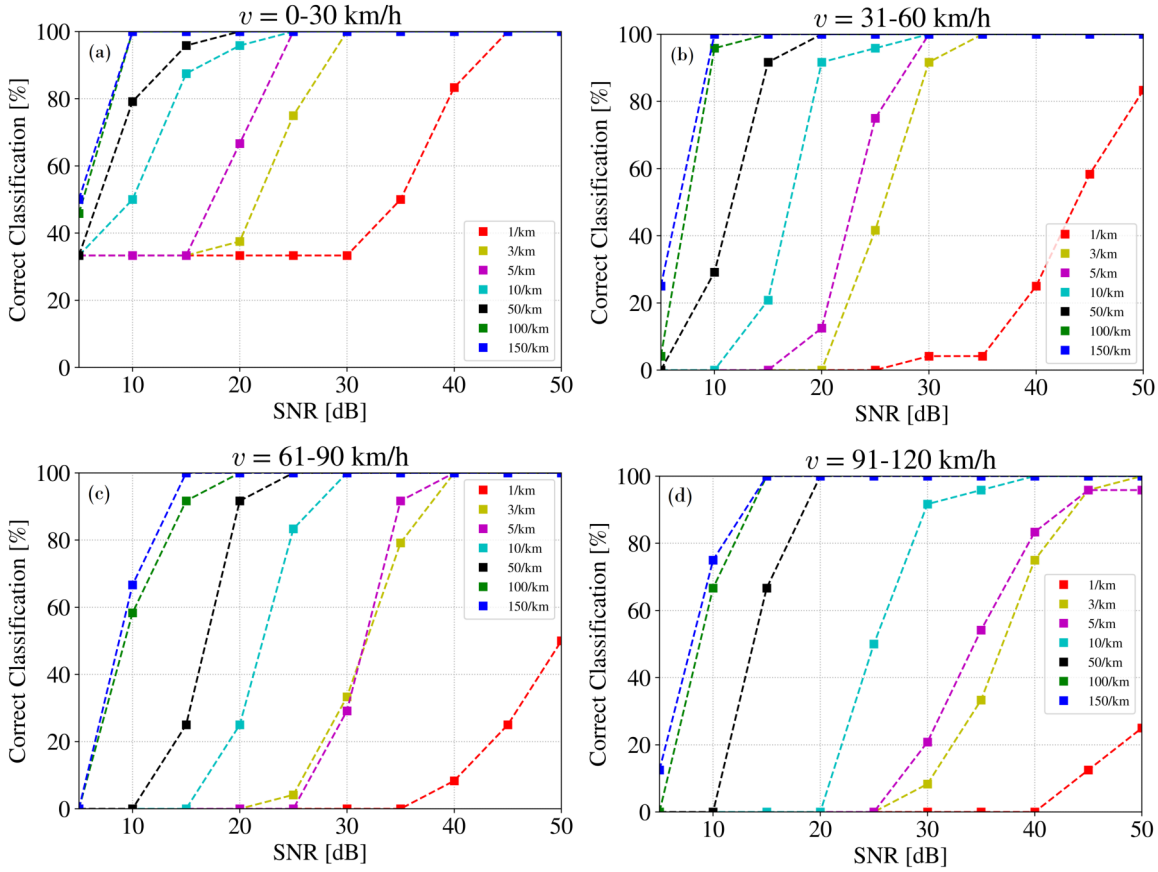

Fig. 9: Impact of car speeds on the classification accuracy. Accuracy is impaired for low car densities and high car speeds because of low resolution in the collected traces.

REFERENCES

[1] A. J. Rogers, "Distributed optical-fibre sensors for the measurement of pressure, strain and temperature," in *Phys. Rep.*, vol. 169, no. 2, pp 99-143, 1988.

[2] A. Barrias, J. Casas, and S. Villalba, "A review of distributed optical fiber sensors for civil engineering applications," in *Sensors*, vol. 16, no. 5, paper 748, 2016.

[3] T. J. Xia *et al.*, "First proof that geographic location on deployed fiber cable can be determined by using OTDR distance based on distributed fiber optical sensing technology," 2020 Opt. Fiber Commun. Conf. Exhib. (OFC), San Diego, CA, USA, 2020, pp. 1-3.

[4] Y. Aono, E. Ip and P. Ji, "More than communications: environment monitoring using existing optical fiber network infrastructure," 2020 Opt. Fiber Commun. Conf. Exhib. (OFC), San Diego, CA, USA, 2020, pp. 1-3.

[5] G. Hancke, B. Silva, and G. Hancke, Jr., "The role of advanced sensing in smart cities," in *Sensors*, vol. 13, no. 1, pp. 393–425, 2012.

[6] R. Tucker *et al.*, "Connected OFCity: technology innovations for a smart city project," in *IEEE/OSA J. Opt. Commun. Netw.*, vol. 9, no. 2, pp. A245-A255, Feb. 2017, doi: 10.1364/JOCN.9.00A245.

[7] F. Peng, N. Duan, Y. Rao and J. Li, "Real-time position and speed monitoring of trains using phase-sensitive OTDR," in *IEEE Photon. Technol. Lett.*, vol. 26, no. 20, pp. 2055-2057, Oct. 2014, doi: 10.1109/LPT.2014.2346760.

[8] Y. Rao, Z. Wang, H. Wu *et al.*, "Recent advances in phase-sensitive optical time domain reflectometry (ϕ-OTDR)," in *Photonic Sens.* 11, pp 1–30 (2021), doi: 10.1007/s13320-021-0619-4

[9] G. A. Wellbrock *et al.*, "First field trial of sensing vehicle speed, density, and road conditions by using fiber carrying high speed data," 2019 Opt. Fiber Commun. Conf. Exhib. (OFC), San Diego, CA, USA, 2019, pp. 1-3.

[10] M. -F. Huang *et al.*, "First field trial of distributed fiber optical sensing and high-speed communication over an operational telecom network," in *J. Lightw. Technol.*, vol. 38, no. 1, pp. 75-81, Jan. 2020, doi: 10.1109/JLT.2019.2935422.

[11] W. Seo, "Fiber optic intrusion sensor investigation," Ph.D. dissertation, Depart. Electr. Eng., Texas A&M University, College Station, TX, USA, 1993.

[12] A. Masoudi and T. P. Newson, "Analysis of distributed optical fibre acoustic sensors through numerical modelling," in *Opt. Express* 25, pp. 32021–32040, Dec. 2017.

[13] L. B. Liokumovich, N. A. Ushakov, O. I. Kotov, M. A. Bisyarin and A. H. Hartog, "Fundamentals of optical fiber sensing schemes based on coherent optical time domain reflectometry: signal model under static fiber conditions," in *J. Lightw. Technol.*, vol. 33, no. 17, pp. 3660-3671, Sep. 2015, doi: 10.1109/JLT.2015.2449085.

[14] X. Lu and P. J. Thomas, "Numerical modeling of ϕ-OTDR sensing using a refractive index perturbation approach," in *J. Lightw. Technol.*, vol. 38, no. 4, pp. 974-980, Feb. 2020, doi: 10.1109/JLT.2019.2949624.

[15] D. Marcuse, *Principles of Optical Fiber Measurements*. New York, NY, USA: Academic Press, 1981.

[16] X. Lu, "Coherent Rayleigh time-domain reflectometry: novel applications for optical fibre sensing," Ph.D. dissertation, Inst. Electr. Eng., Swiss Federal Inst. Technol. Lausanne, Lausanne, Switzerland, 2016.

[17] F. Chollet. *Deep Learning with Python*. Greenwich, CT, USA: Manning Publications, 2017.

[18] C. M. Bishop. *Pattern Recognition and Machine Learning*. New York, NY, USA: Springer, 2006.

[19] X. Lu and K. Krebber, "Characterizing detection noise in phase-sensitive optical time domain reflectometry," *Opt. Express* 29, pp. 18791-18806, 2021.

[20] K. De Souza and T. P. Newson, "Signal-to-noise and range enhancement of a Brillouin intensity based temperature sensor," *Opt. Express* 12, pp. 2656-2661, 2004.

[21] X. Angulo-Vinuesa, A. Dominguez-Lopez, A. Lopez-Gil, J. D. Ania-Castañón, S. Martin-Lopez and M. Gonzalez-Herraez, "Limits of BOTDA range extension techniques," in *IEEE Sensors J.*, vol. 16, no. 10, pp. 3387-3395, May 2016, doi: 10.1109/JSEN.2015.2424293.

[22] S. Liu, F. Yu, R. Hong, W. Xu, L. Shao *et al.*, "Advances in phase-sensitive optical time-domain reflectometry," in *Opto-Electron. Adv.*, vol. 5, no. 3, paper 200078, 2022. doi: 10.29026/oea.2022.200078